Synchrotron radiography characterization of the liquid core dynamics in a canonical two-fluid coaxial atomizer

Nathanael Machicoane [a,*], Julie K. Bothell [b], Danyu Li [b], Timothy B. Morgan [b], Theodore J. Heindel [b], Alan L. Kastengren [c], Alberto Aliseda [a]

[a] University of Washington, Department of Mechanical Engineering, Seattle, WA 98105, USA
[b] Iowa State University, Department of Mechanical Engineering, Ames, IA 50011, USA
[c] Energy Systems Division, X-ray Science Division, Advanced Photon Source, Argonne National Laboratory, Argonne, IL 60439, USA

ABSTRACT

The liquid core of a canonical two-fluid coaxial atomizer has been characterized using synchrotron X-rays. The high energy photons allow for high-speed imaging of attenuation through the dense liquid-gas jet core, resolving the internal structures that include entrapped air bubbles and the formation of liquid ligaments and bags. When the gas-to-liquid momentum ratio increases, the liquid core transitions from an intact column, where primary break-up happens several liquid diameters downstream, to a hollow crown with a downstream span comparable to the liquid diameter that disintegrates by shedding ligaments from its rim. At high gas momentum ratios (limited by the sonic velocity at the gas nozzle exit), this crown suffers partial dewetting and, when angular momentum is added to the gas, it dewets on a large section of the liquid injection needle circumference. This partial crown exhibits azimuthal motions along the circumference, on timescales much longer than the relevant flow timescales. The crown attachment to the liquid needle presents a bi-stable nature. The dramatic changes of the liquid core morphology, as the gas momentum and swirl ratios vary, have a strong impact on the gas-liquid boundary layers, which control the liquid break-up mechanisms and the resulting spray characteristics, such as droplet size distributions and the droplet volume fraction across the spray.

© 2019 Elsevier Ltd. All rights reserved.

1. Introduction

The destabilization and subsequent break-up of a liquid jet by a co-flowing high-speed gas is a fundamental multiphase flow problem with many industrial and practical applications. Despite its extensive use, some underlying physical mechanisms are still not yet fully understood, making prediction of spray characteristics difficult and uncertain. For coaxial two-fluid atomizers, different modes of atomization have been identified in regimes where the gas dominates the break-up process (Lasheras and Hopfinger, 2000; Marmottant and Villermaux, 2004). In the lower range of the gas momentum ratio, a sinusoidal instability suddenly exposes the liquid to high gas stresses and results in bag break-up, producing a very heterogeneous droplet distribution as the bag film yields much finer droplets than its rim. At intermediate gas momentum ratios, varicose instabilities that further destabilize into ligaments and then droplets are the results of

the liquid jet acceleration within the potential cone of the gas. At higher gas momentum ratios, ligaments are formed through a Kelvin-Helmholtz instability and quickly suffer from a subsequent Rayleigh-Taylor instability breaking them into small droplets, in what is referred to as fiber-type atomization. The thickness of the gas boundary layer along the liquid intact core has been proven to be a determining parameter for droplet size in the far field of the spray after secondary break-up takes place (Lasheras et al., 1998; Varga et al., 2003; Aliseda et al., 2008).

Recently, a linear stability analysis combined with an extensive experimental study has shown that both the gas and liquid boundary layer thicknesses drive the frequency of the sinusoidal instability experienced by the liquid core, often referred to as flapping (Delon et al., 2018). The measurements of the boundary layer thickness are frequently collected with only one phase present, or are modeled. The presence of both phases, which are effectively coupled in the parallel flow at the nozzle exit, impacts the boundary layer thicknesses significantly. In the absence of two-phase boundary layer measurements that are not currently available, a better understanding of the liquid core state would help bridge single-phase boundary layer models closer to the actual

multiphase interfacial instability. This basic physical understanding can also help better predict, in a quantitative manner, the effects of open-loop actuation deployed on the spray, such as the addition of angular momentum in the gas to enhance spreading and improve break-up (Hopfinger and Lasheras, 1996; Machicoane et al., 2018).

The near-field of a spray is a high liquid volume fraction region, where classical imaging techniques fail to reveal a comprehensive picture. Ballistic imaging and X-ray radiography have recently shown the potential for insights because they can penetrate the dense multiphase flow with visible light and X-ray photons, respectively (Linne et al., 2009; Yue et al., 2001; Heindel, 2011). Synchrotron X-rays, like the ones produced at Argonne National Laboratory's Advanced Photon Source (APS), provide a high-flux collimated beam that can be used to probe the spray with high spatial and temporal resolution, even in its densest regions (Kastengren and Powell, 2014; Heindel, 2019). This study uses the unique capability of synchrotron radiography to image the dense near-field region of a canonical coaxial two-fluid atomizer. Experiments are performed under a wide range of parameters to provide better understanding of the liquid core that can be leveraged into quantitative models for prediction of spray droplet size and spatial distribution.

The paper is organized as follow: the canonical atomizer and the synchrotron X-ray imaging setup are presented in Section 2. Qualitative observations of the spray in the near-field region for a wide range of flow parameters are then made in Section 3. Section 4 presents quantitative measurements of the liquid core temporal dynamics and a phase diagram of the different states identified for the near region, which are then discussed in Section 5. The conclusions of the study and the potential for future investigation based on this exciting new measurement technique are summarized in Section 6.

2. Experiment setup

2.1. A canonical atomizer

A two-fluid coaxial atomizer has been designed to study atomization physics in a canonical setting, with well characterized and reproducible laminar liquid and turbulent gas streams (see Huck et al. (2018) for more details). The nozzle design as well as its manufacturing procedure, including the complete 3D geometry that can be used for numerical simulations, is open-source and available to the community at http://depts.washington.edu/fluidlab/nozzle.shtml. As sketched in Fig. 1, the liquid is injected at a fixed flow rate Q_l via a straight circular needle, yielding a fully developed Poiseuille flow at the outlet of the nozzle where it is atomized by the coaxial gas jet. The gas enters the nozzle through its sidewalls, perpendicular to the axis of the atomizer through eight inlets. It then flows longitudinally along the axis of the nozzle, whose inner (the outer wall of the liquid needle) and outer surfaces are cubic-spline shaped. Four inlets impinge onto the nozzle longitudinal axis, across the four quadrants, producing a purely coaxial gas stream, while the four other inlets are off-axis, introducing angular momentum in the gas stream. The gas injection inlets are denoted no-swirl (NS) and swirl (SW), respectively, and the gas flow rate is $Q_{Total} = Q_{NS} + Q_{SW}$. When swirl is added to the gas, the total flow rate is kept constant, diverting part of the total gas from the no-swirl to the swirl injection. The magnitude of swirl in the gas is defined as the swirl ratio: $SR = Q_{SW}/Q_{NS}$, and $0 < SR < 1$ in this study.

The liquid and gas mean exit velocities are defined as $U_l = Q_l/A_l$ and $U_g = Q_{total}/A_g$, where $A_l = \pi d_l^2/4$ and $A_g = \pi(d_g^2 - D_l^2)/4$ are the liquid and gas nozzle areas respectively, and $d_l = 2.1$ mm, $D_l = 2.7$ mm and $d_g = 10$ mm are the liquid needle inner and outer diameters (measured from the X-rays radiographs of the nozzle exit) and the gas nozzle inner diameter, respectively. The gas-to-liquid momentum ratio $M = \rho_g U_g^2/\rho_l U_l^2$, which compares the dynamic pressure of the gas to the liquid's, is always greater than 1, while the liquid mass loading $m = \rho_l A_l U_l/\rho_g A_g U_g$ is much smaller than unity for the conditions investigated. The fluid densities and kinematic viscosities are ρ_i and ν_i, respectively, with subscript l and g for liquid and gas; the surface tension is σ. Table 1 lists the parameters under which the effect of the momentum ratio is studied, keeping the liquid Reynolds number constant and within the laminar regime, $Re_l = 4Q_l/\pi d_l \nu_l = 1100$. The effect of varying the liquid Reynolds number (spanning the laminar and turbulent regimes below and above the critical Reynolds number for pipe flow equal to 2300, Tennekes and Lumley (1972)), while keeping the gas-to-liquid moment flux ratio constant, is explored with the operating parameters shown in Table 2.

The gas Reynolds number $Re_g = 4Q_g/\pi d_{eff}\nu_g$ (where $d_{eff} = \sqrt{4A_g/\pi}$) ranges from approximately $2\,10^4$ to $2\,10^5$. The Weber number, based on the exit velocities and the liquid inner diameter, $We_{d_l} = \rho_g(U_g - U_l)^2 d_l/\sigma$ spans between 30 and 3000.
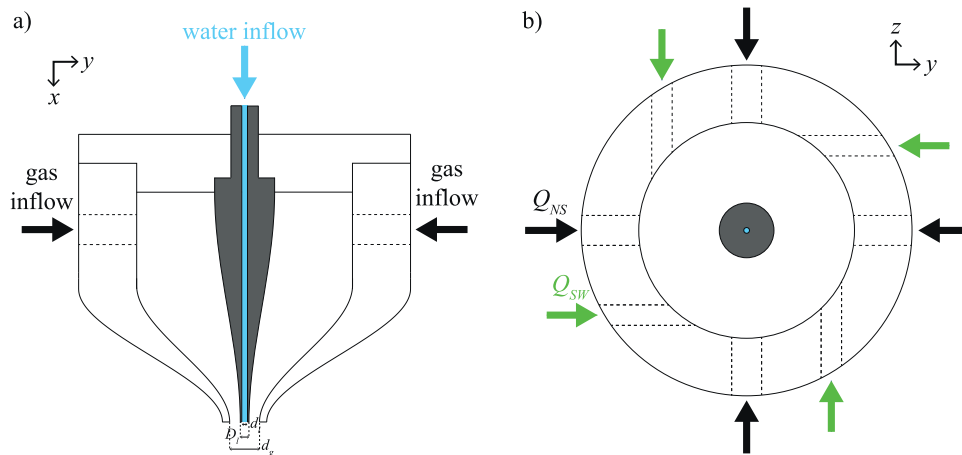

Fig. 1. Schematic of the coaxial two-fluid atomizer along a longitudinal cut (a) and transverse cut at the inlets plane (b). The longitudinal (vertical) axis is denoted x while the transverse axes are y and z. Water enters the nozzle through a long vertical straight needle while gas flows in through 8 horizontal inlets, perpendicular to the flow direction, and along the cubic-spline shaped inner and outer wall of the nozzle. Four inlets are on-axis and produce a longitudinal gas co-flow while four others are off-axis and induce swirling motions. (For interpretation of the references to colour in this figure legend, the reader is referred to the web version of this article.)

Table 1

Flow parameters for a fixed liquid Reynolds number $Re_l = 4Q_l/\pi d_l \nu_l = 1100$, varying the gas Reynolds number $Re_g = 4Q_g/\pi d_{eff} \nu_g$. The gas-to-liquid momentum ratio is $M = \rho_g U_g^2/\rho_l U_l^2$, the liquid mass loading is $m = \rho_l A_l U_l/\rho_g A_g U_g$ and the Weber number is based on the liquid diameter as $We_{d_l} = \rho_g (U_g - U_l)^2 d_l/\sigma$. The fluids are air and distilled water, at an ambient temperature of 25° C, with kinematic viscosities of $\nu_g = 1.56\ 10^{-5}$ m^2 s^{-1} and $\nu_l = 8.96\ 10^{-7}$ m^2 s^{-1}, densities $\rho_g = 1.18$ kg m^{-3} and $\rho_l = 996.9$ kg m^{-3}, and the water surface tension $\sigma = 72$ mN m^{-1}. The swirl ratio $SR = Q_{SW}/Q_{NS}$ for each conditions was either 0, 0.5 or 1, and the values 0.25 and 0.75 were also explored for $M = 28.9$.

Re_g	M	m	We_{d_l}
21 200	6	0.56	39
46 500	28.9	0.25	192
83 400	92.9	0.14	620
123 000	202	0.1	1350

Table 2

Flow parameters to study the impact of varying gas and liquid Reynolds numbers while keeping the momentum ratio constant at 3 different values.

M	Re_l	Re_g	We_{d_l}
6	1100	21 200	39
6.1	6500	123 000	1320
28.4	4400	180 000	2850
28.5	2300	93 000	771
28.6	3000	123 000	1340
92.9	1100	83 400	620
94.1	1600	123 000	1350

2.2. High-speed X-ray imaging

Synchrotron X-ray radiography of the atomizer and resulting spray was performed in the Advance Photon Source (APS) at Argonne National Laboratory, 7-BM beamline (Kastengren et al., 2012). It provides high-intensity broadband X-rays that can be used for 2D radiographic imaging with microsecond or sub-microsecond time resolution (Halls et al., 2017). Such radiography is often referred to as white beam imaging because the energy spectra of the illuminating beam is distributed over a broadband of wavelengths. The high-intensity continuous wave beam allows for high resolution measurements in space (high magnification) and time (high frame rate, short exposure). Depending on the momentum ratio, image acquisition was completed at 6000 or 10,000 frames per second, while keeping a constant exposure time of 1.05 μs, corresponding to spatial resolutions of 608 × 512 pixels or 512 × 256 pixels, respectively, to capture primary break-up events of the spray. Due to the beam's high energy density (0.6 W mm^{-2}), a chopper wheel is used, preventing significant heating of the nozzle and scintillator. The chopper wheel has two openings to let the beam through and rotates at 2 Hz. This results in image sequences between of 200 and 300 consecutive frames (30 ms duration at 6000 or 10,000 fps), separated by about 250 ms without signal from the spray. The field of view are either 5.8 mm × 4.9 mm or 4.9 mm × 2.4 mm, depending on the frame rate of acquisition. The nozzle is sequentially displaced with respect to the fixed beam to image different regions of interest in the spray. This is done by forming a mosaic of overlapping fields of view of the imaging system with respect to the nozzle as it is traversed in the plane perpendicular to the X-ray beam, by a two-dimensional translation stage system (position accuracy and repeatability better than 5 μm). This imaging arrangement, using a collimated X-ray beam, is schematically shown in Fig. 2 (more details can be found in Heindel et al. (2017); Bothell et al. (2018)).

The X-ray beam is attenuated as it passes through the spray (propagating along the z axis), following Beer-Lambert absorption law $I = \int I_0 e^{-\mu(\lambda)l} d\lambda$ (where I_0 is the initial beam intensity and I
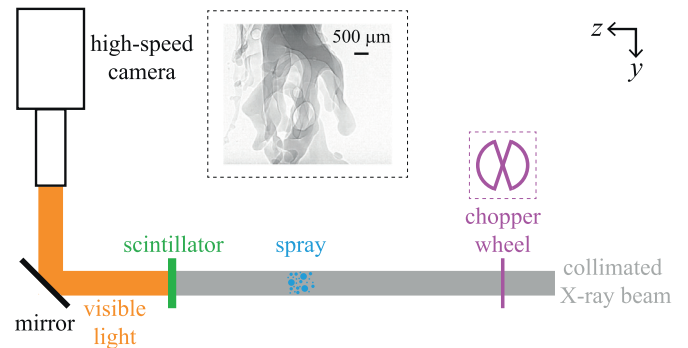

Fig. 2. Schematics of the synchrotron X-ray imaging arrangement. The 7-BM beamline at APS provides a collimated X-ray beam, whose cross-section is approximately 8 mm by 6 mm, that goes through the spray, being partially absorbed. The beam then reaches a scintillator crystal, that re-emits visible light proportional to the X-ray beam intensity, which is captured by a high-speed camera after it reflects on a 45° mirror. A combination of two lenses permits a magnification ratio of 2. A typical snapshot is shown in the black dashed line box. A chopper wheel, which is pictured sideway in the purple dashed line box, prevents overheating of the scintillator and the nozzle by the intense X-ray beam. (For interpretation of the references to colour in this figure legend, the reader is referred to the web version of this article.)

is the intensity after the beam has been absorbed by an equivalent path length of fluid l with an absorption coefficient μ that depends on the wavelength λ). After crossing the spray domain, the attenuated beam shines onto a 500 μm thick YAG:Ce scintillator crystal that fluoresces visible light proportionally to the X-ray intensity. This visible light is recorded using a high-speed camera focused on the scintillator surface through a 2X magnification lens arrangement. The camera views the scintillator via a 45° mirror to avoid damage to the camera sensor caused by slightly refracted X-rays propagating behind the scintillator. Because of the broadband nature of the X-ray beam and the dependency of the absorption coefficient μ on wavelength, the visible light intensity recorded by the high-speed imaging is not exactly proportional to the length of liquid it has traversed. However, the intensity of each pixel in the 2D images is representative of the optical depth. Determining the equivalent path length requires a complex calibration procedure unlike the simple μ calculation for monochromatic X-ray attenuation. Thus, the image intensity quantifies the quantity of liquid in the spray sampled in the transverse direction, z, so that the liquid jet inner structure during break-up is clearly visible in a manner not possible with visible light measurements (see inset of Fig. 2).

3. Qualitative observations

Synchrotron high-speed X-ray imaging provides a detailed picture of the liquid core structure and the instabilities that lead to primary break-up with very high spatial and temporal resolutions. Fig. 3 shows white beam radiographic images of the spray near field, just downstream of the nozzle exit, at increasing values of gas momentum ratio and different swirl ratios. Even at low values of the momentum ratio, $M = 6$, when the spray near-region structure is less complex, this imaging technique shows a clear advantage in the information captured by the high-speed X-ray videos, compared to classical visible light illumination approaches. The latter shows only the surface of the liquid core as it is perturbed by instabilities and forms waves or bags. Conversely, synchrotron radiographies, as shown in Fig. 3, detect the projection of three-dimensional small-scale structures, with liquid sheets forming and folding. These events often result in either a local tear in the liquid sheet or, unexpectedly, in the entrapment of air bubbles within the liquid core. These bubbles are advected downstream (see Fig. 3c-d)) and can persist in very thin liquid ligaments, sheets or even inside liquid droplets resulting from
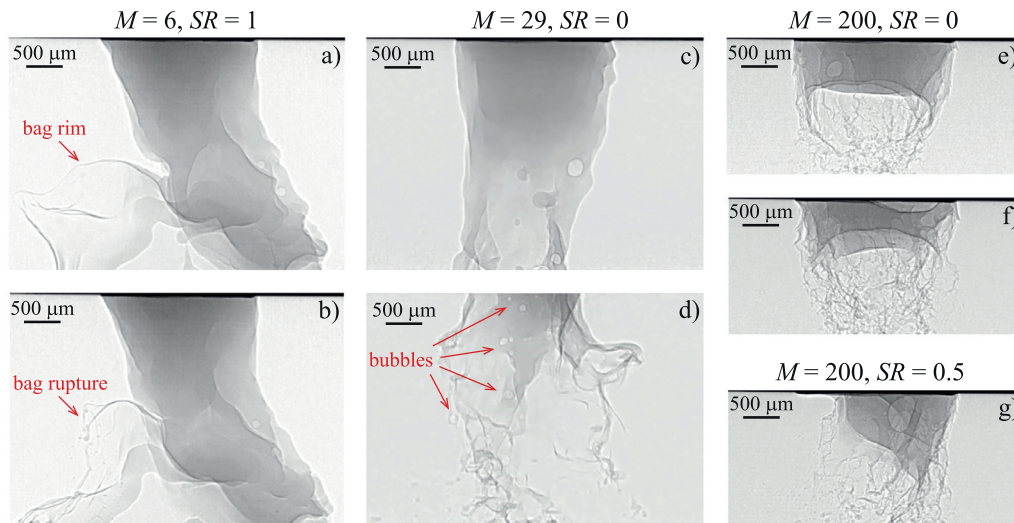
Fig. 3. Instantaneous radiographic images of the spray near-field. The black band across the top ($x = 0$) of all images (except d)) is the nozzle exit, with the water needle wall protruding slightly at the nozzle vertical axis of symmetry ($y = 0$). (a-b) Two quasi-consecutive frames (1 ms time interval) taken at momentum ratio $M = 6$ and swirl ratio $SR = 1$, showing bag breaking. (c-d) Two uncorrelated frames of the spray near-field, (c) is at the nozzle exit, $x = 0$, while (d) images the next downstream location ($x = 0.75d_l$) at momentum ratio $M = 29$ and, $SR = 0$ showing bubble entrapment within the liquid intact core that persist into sheets as they formed further downstream. (e-f) Two consecutive frames taken at momentum ratio $M = 200$ and $SR = 0$ showing the formation of a crown at the liquid injection, with partial dewetting of the needle rim visible in (f). (g) Single image taken at momentum ratio $M = 200$ and $SR = 0.5$ showing a strongly asymmetric unstable crown as its attachment length (about $120°$ wide for this M and SR conditions) moves azimuthally around the perimeter of the needle. In this frame the liquid is attached only on the right side of the needle. The field of view imaged is $2.2d_l \times 1.5d_l$ for (a-d) and $1.9d_l \times 0.9d_l$ for (e-f). (For interpretation of the references to colour in this figure legend, the reader is referred to the web version of this article.)

break-up (see, for example, the video at https://gfm.aps.org/meetings/dfd-2017/59b14ed7b8ac316d38841a94/ at time stamp 2:24). This may result in changes in the break-up mechanisms for sheets or ligaments, as the bubbles alter the energy balance to perturb and pierce the liquid-core/outer gas interface.

For higher values of the momentum ratio, the shape of the liquid core changes drastically (Fig. 3e-f)), with the high momentum gas accelerating a thin layer around the rim of the liquid. This process forms a hollowed-out core that evolves, within one liquid jet diameter, into a liquid crown from which ligaments form and break-up. This process involves the gas jet separating in the wake of the liquid core and producing a downstream recirculation cavity that creates highly dynamic perturbations on the liquid crown, placed in the high shear region between the high-speed outer gas and the low-speed recirculating gas that fills the volume downstream of the liquid needle. Bubble entrapment is still observed,

but bubble lifetimes are much shorter. Gas instabilities lead to partial de-wetting of the liquid needle circumference by the liquid crown, as observed on Fig. 3f). In the presence of swirl, the recirculating gas instabilities are stronger and can lead to de-wetting with a larger spatial extent along the liquid needle circumference, with the crown's attachment length rotating azimuthally at frequencies consistent with the separation bubble instability induced by the swirling outer gas. The liquid crown moves slowly compared to the spray timescales, staying in the same quadrant of the needle perimeter longer than the period of consecutive image acquisition (20-30ms). In subsequent acquisitions of the same spray, the crown is found attached at other locations along the perimeter, with approximately the same length of attachment ($\approx 120°$). The nozzle is axisymmetric and no distinction is found among positions of attachment along the liquid needle circumference. We call this regime the unstable crown break-up regime. Fig. 4 shows
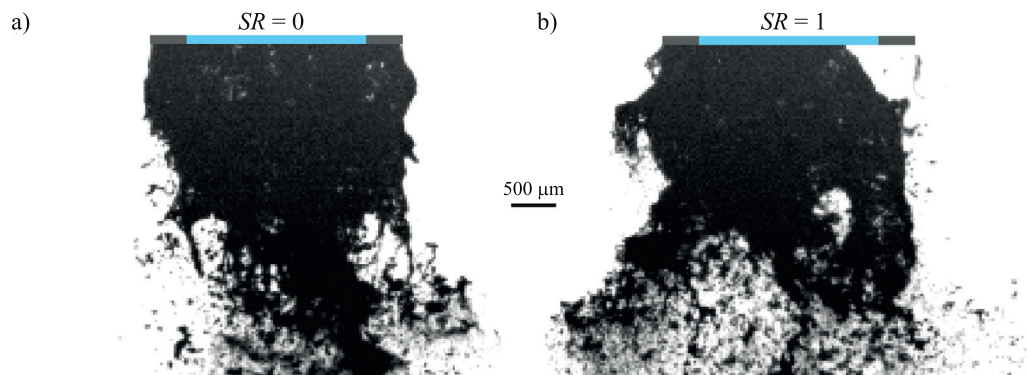

Fig. 4. Instantaneous back-lit images of the spray near-field. The liquid needle is represented with the gray rectangle with a blue one embedded standing for the needle inner part where liquid is injected. Momentum ratio $M = 93$ and swirl ratio $SR = 0$ (a) and $SR = 1$ (b), respectively in a crown and unstable crown regime of the liquid core. The field of view imaged is $3d_l \times 2d_l$. (For interpretation of the references to colour in this figure legend, the reader is referred to the web version of this article.)
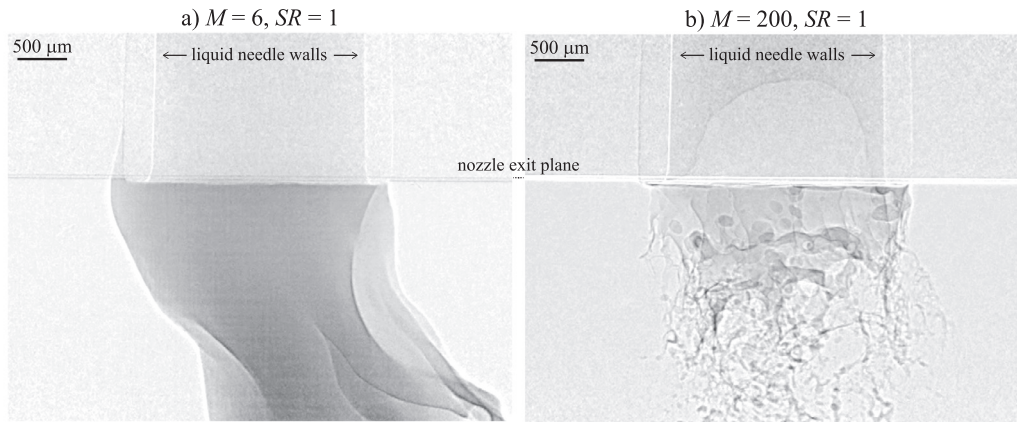
a) $M = 6$, $SR = 1$ b) $M = 200$, $SR = 1$

Fig. 5. Instantaneous radiographic images showing both the outside and the inside of the atomizing nozzle. The horizontal line seen approximately at one third of the image from the top represents the nozzle exit plane. Inside the atomizer, starting from the axis of symmetry at the center of the frame and moving radially outwards, we find the liquid inside the injection needle represented by the darker region corresponding to high absorption by the liquid, then we can see the walls of the liquid needle, and finally the volume occupied by the gas inside the nozzle (only the gas nozzle wall attenuation is visible in the images, the edge of the gas nozzle is not in the field of view). The image dimensions are $2.6d_l \times 1.9d_l$. (a) Momentum ratio $M = 6$ and swirl ratio $SR = 1$. Liquid wetting the outer wall of the water needle upstream of the injection plane. The sinuous flapping of the liquid results in this wicking behaviour, despite the high-speed gas flow inside the gas nozzle. At the liquid position in the gas boundary layer (100 μm from the solid wall) the gas mean velocity is nominally 10 ms^{-1}. The swirl on the gas leads to separation along the tapered liquid needle wall and a low pressure region just upstream of the liquid injection that drives this liquid motion upstream from the injection. (b) Momentum ratio $M = 200$ and swirl ratio $SR = 1$. Gas recirculation inside the liquid needle, penetrating the liquid crown along a large fraction of the needle exit perimeter, consistent with the view of the liquid in Fig. 3g). A recirculation cavity for the gas is created inside the liquid needle, with estimated width and depth $0.8d_l \times 0.5d_l$ (from attenuation measurements in the direction of propagation of the X-ray beam), forcing the water to accelerate inside the needle and exit along about half of the inner cross section of the liquid needle. (For interpretation of the references to colour in this figure legend, the reader is referred to the web version of this article.)

conditions with a stable and unstable crown obtained with back-lit high-speed imaging for comparison. While some features are still observable, such as the crown de-wetting, the hollow character of the liquid core cannot be assessed with such classical light imaging technique. Comparing Fig. 4 to Fig. 3 clearly shows the advantage of using white beam imaging for near-field characterization.

Synchrotron X-rays penetrate the gas nozzle and liquid needle walls, allowing for instantaneous measurements of the liquid flowing inside the aluminum atomizer. This provides a view of the wetting dynamics of the liquid on the needle. Under low mass ratio conditions, the liquid fully wets that frontal edge of the needle, so that the liquid jet diameter, when it first encounters the gas, is the outer needle diameter, $D_l = 2.7$ mm. At high swirl ratios (and low momentum ratio), the liquid is observed to wick up the outer wall of the needle (Fig. 5a). Wicking up to 250 μm upstream of the needle exit plane can be observed, with local film thickness up to 200 μm (see the video at https://gfm.aps.org/meetings/dfd-2017/59b14ed7b8ac316d38841a94/ at time stamp 0:43 s). These wicking events are intermittent, with duration of the order of 5 ms, but have been observed to last up to 20 ms.

Another unexpected phenomenon, that becomes observable thanks to the synchrotron high-speed X-ray radiography, is gas penetrating inside the liquid needle (Fig. 5b)). At high swirl and momentum ratios (over 0.5 and 90 respectively), a highly dynamic gas cavity forms inside the water needle (see the video at http://depts.washington.edu/fluidlab/FEDSM2017video.shtml at time stamp 1:48 s). The gas penetrates upstream about half a liquid diameter, and it is common to observe this phenomenon for times longer than the acquisition time of 30 ms (limited by the chopper wheel). Occasionally, the gas cavity is short-lived and forms and collapses within 5 ms in the recorded image sequence. At high values of the swirl ratio, $SR = 1$, the gas cavity occupies a large fraction of the liquid needle cross-section, forcing the liquid to exit through a small, crescent moon cross-section. This results in a very asymmetric crown visible on the outside of the liquid needle (Fig. 3g). The unsteady cavity collapses at high frequencies and forms immediately at another azimuthal location inside the needle, yielding the unstable crown regime described previously.

4. Characterization of the spray near-field

4.1. Dynamics of the unstable crown regime

As described above, the attachment length of the unstable crown never stabilizes along the needle perimeter. Due to the projection of the liquid length onto the imaging plane, it is not possible to distinguish between the liquid crown being on the front or the back of the needle with respect to the X-ray beam (center of mass located on a positive or negative z position). Thus, the characterization of the unstable crown is done by the transverse location of its center of mass, in a periodic interval of 180 degrees along the needle perimeter. Fig. 6a-b) shows the calculation of the center of mass of the liquid crown, Y_m, (the image intensity-weighted
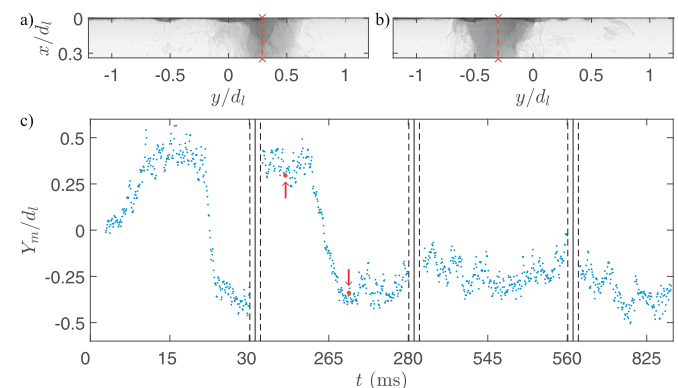

Fig. 6. (a-b) X-ray images for a momentum ratio $M = 200$ and a swirl ratio $SR = 1$. The vertical red dashed line shows the instantaneous center of mass of the unstable liquid crown along the transverse direction y, denoted as Y_m. (c) Center of mass transverse location Y_m/d_l as a function of time t. The vertical black lines surrounded by dashed lines show the time discontinuities separating 250 ms-long runs. The two successive bigger red dot (indicated by arrows) corresponds to the value of Y_m for Fig. (a) and (b), respectively. (For interpretation of the references to colour in this figure legend, the reader is referred to the web version of this article.)

average y position, integrated across the extent of the image in the x-axis, for two instants within the same image sequence. The crown shifts from the image right or the left ($M = 200$, $SR = 1$), representing a switch in the azimuthal angle for the attachment of the liquid crown along the perimeter from the first (or fourth) quadrant, $0 - \pm 90°$, to the second (or third) quadrant, $\pm 90 - \pm 180°$. Fig. 6c) displays the time evolution of the crown's center of mass location, Y_m, for several consecutive acquisitions, representing the rotation of the crown along the needle perimeter. On the first run, the residence time on the first/fourth quadrant, $Y_m \geq 0$ is 12 ms, with a very rapid transition from positive to negative y (from right to left on the image) in 1.9 ms. The second run starts at 250 ms and shows a similar fast transition from positive to negative Y_m, in approximately 5 ms. The overall rotation speed is high in these two first runs, while the two subsequent runs, starting at 530 ms and 810 ms, respectively, show the center of mass at a steady location, for the length of the image sequence, 30 ms. Thus, the rotation of the crown attached to liquid needle perimeter is unsteady and the attachment location rotational speed varies with time in a chaotic manner. More sequences for the same atomization conditions, or longer sequences would be needed to characterize the possible natural frequencies of the instability, or the chaotic state space.

From the temporal evolution (approximately 30 independent runs) of the transverse location of the liquid core center of mass, Y_m, we compute the probability density functions (PDF) to understand the azimuthal location (projected onto the y axis) of the liquid crown. Fig. 7a) shows, for a momentum ratio $M = 200$, how addition of swirl introduces a partial, unstable crown. The PDF shape for the no swirl $SR = 0$ case is a single mode distribution centered at $y = 0$, representing a full azimuthal crown. When swirl is present, the PDF switches to a bi-modal distribution representing a partial crown that rotates around the needle perimeter. For $SR = 0.5$, the crown fills a significant part of the needle, with the PDF modes on $Y_m^{mode} = \pm 0.15 d_l$ and a probability 1.5 times greater than at the centerline $y = 0$. This is possible because the liquid crown extends for more than half of the perimeter, $> 180°$, so that the center of mass is more frequently near the front or back (which have a longer projected length onto the X-ray image) than on the sides (with a much shorter projected length). The mode location moves significantly closer to the outer edge of the liquid needle for $SR = 1$, $Y_m^{mode} = \pm 0.33 d_l$. It represents a switch to a much shorter attachment length, $< 120°$, accompanied by a drastic increase of the rotational speed of the crown (so the short crown is frequently found along on the outer edge in the image, ≈ 0 or $180°$, where there is a high probability of projecting on, and less frequently along the center of the image $y \approx 0$, where there is a much more evenly distributed probability).
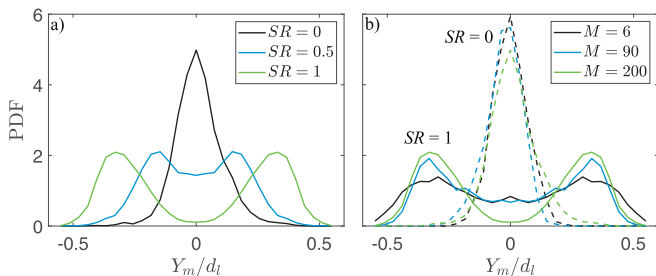
Fig. 7(b) shows that for any value of the momentum ratio in the absence of swirl, the liquid core (that can be intact or a crown with or without partial dewetting) is always fully anchored, having a PDF peak at $Y_m = 0$, and decreasing very steeply towards the outer edge of the needle perimeter. The slight flattening of the PDF when M increases is due to the increased instability of the liquid core, that makes its center of mass oscillate around $Y_m = 0$. When swirl is added, the PDF changes drastically for all values of the momentum ratio. As described above, at high values of M this is due to the liquid crown becoming unstable, dewetting the needle circumference and experiencing rotational motion with frequencies lower than 30 Hz (periods longer than the image sequence length of 30 ms). It is important to note that dewetting happens much more often at high values of the momentum ratio; the highest probability peak is 3 times higher at the sides than at the center for $M = 90$, while it is 20 times higher for $M = 200$. For low values of the momentum ratio, the PDF is almost uniform, with a highest to lowest probability ratio being only 2. The bi-modal nature of the PDF for the low momentum ratio, $M = 6$, where the liquid core does not form a crown and is always fully attached to the needle perimeter, is due to the effect of swirl on the sinusoidal instability of the intact liquid core, associated with the wicking up the needle walls. Fig. 5(a) can be interpreted in this light to produce a center of mass displaced to large ($Y_m \geq 0.25 D_l$) positive values of the y coordinate.

4.2. Entrapped air bubbles

From the collection of instantaneous images, we produce a first quantitative characterization of the air bubble entrapment by the liquid core. We compute the projected area of bubbles when they are present in the images. This area is non-dimensionalized by the instantaneous projected area covered by the liquid core on the image. This non-dimensional area, averaged over the total number of images, is plotted on Fig. 8, representing an average projected surface fraction of bubbles in the core. Note that if a bubble appears in multiple successive images, it is only counted only once, so as not to bias the measurement due to slow large bubbles.

As the spray becomes more unsteady, i.e. when the momentum ratio increases, the projected bubble area fraction tends to increase. This is be expected as the bubbles get entrapped by sheets of liquid, detaching and reattaching on the surface of the liquid core. For $M = 6$, the addition of swirl increases this fraction, while at the maximum swirl ratio investigated, the value is, surprisingly, almost zero (same as at $SR = 0$). This is in agreement with the visualization of the spray's spreading angle and intact length (Huck et al., 2018): the spray widens and becomes more unstable for $SR = 0.5$, while for $SR = 1$ the core sinusoidal flapping is slightly more unstable, as the flow separation and recirculation
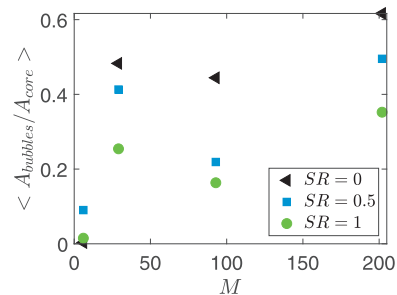

Fig. 7. Probability density functions of the transverse location of the liquid core center of mass, Y_m/d_l. (a) Momentum ratio $M = 200$ and various swirl ratios, where an unstable crown is observed for $SR > 0$. (b) Various momentum ratios in the absence of swirl (dashed lines) and with a swirl ratio $SR = 1$ (continuous line); an unstable crown is observed for $SR = 1$ and $M \geq 90$. (For interpretation of the references to colour in this figure legend, the reader is referred to the web version of this article.)

Fig. 8. Average projected surface area fraction covered by bubbles in the liquid core, computed as the ratio of the average projected area covered by bubbles divided by the average projected area covered by the liquid core on all the images that contain bubbles. (For interpretation of the references to colour in this figure legend, the reader is referred to the web version of this article.)
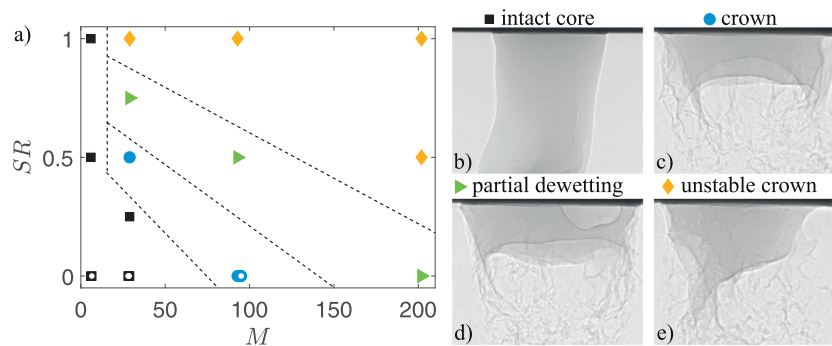
Fig. 9. (a) Phase diagram of the liquid core morphology, established from image analysis. (b) The intact jet corresponds to a liquid column, which can be deformed in sinusoidal or varicose modes, forming bags or ligaments. (c) The crown refers to a liquid core with a hollow center that can extend up to inside the water needle. (d) Partial dewetting implies that the liquid crown detaches on part of the liquid needle perimeter, but the liquid crown is still intact downstream of the detachment, forming a full 360° liquid sheet. (e) Unstable crown corresponds to detachment of the liquid for the larger part of the liquid needle perimeter, where the gas recirculation cavity invades the liquid needle, preventing the liquid core from reaching the full azimuthal liquid needle perimeter. For Figure (a), the filled symbols with a hollow white center correspond to the seven conditions of Table 2, while the filled symbols are from Table 1. The dashed lines are visual guidelines for possible transition values between neighboring shapes. (For interpretation of the references to colour in this figure legend, the reader is referred to the web version of this article.)

induced by the high swirl at this low gas axial momentum confines the spray with limited radial dynamics. At higher values of the gas momentum ratio, increases in swirl consistently decrease the projected bubble surface fraction. We attribute this to the shortened intact liquid core, with a transition towards the unstable crown regime and lower probability of finding bubbles entrained in the liquid *while still an intact core*, but not in droplets, which are not accounted for here.

4.3. Phase diagram of the liquid core morphology

Fig. 9 shows the phase diagram representing the different morphologies observed in the liquid core, in a parameter space defined by the momentum, M, and swirl, SR, ratios. The four morphologies identified have been described above with the corresponding representative X-ray images: intact jet, crown, partially-dewetting crown and, finally, unstable crown. The filled symbols correspond to the conditions summarized in Table 1 for $Re_l = 1100$. In addition, varying liquid Reynolds numbers are also investigated in the absence of swirl, following Table 2, at similar values of the momentum ratio to Table 1, and are represented with hollow white center symbols.

Analysis of the transition regions between the different liquid core morphologies indicates that:

- The addition of swirl makes the crown unstable; in the presence of swirl the crown detaches from the liquid needle at every M, except the lowest $M = 6$, while in the absence of swirl, the spray only experiences partial dewetting for the highest value of the momentum ratio investigated ($M = 200$).
- Gradual transitions are observed when increasing the momentum ratio, compared to sudden changes observed when increasing the swirl ratio above the critical value ($SR = 0.4$ (Hopfinger and Lasheras, 1996)). All four regimes are observed for $M = 29$ at different values of SR, while partial dewetting is only observed in the absence of swirl for large increases in M (multiplied by 7). Without the finer increments in the swirl ratio applied at $M = 29$ ($\Delta SR = 0.25$), the liquid core would experienced a transition directly from intact jet to crown/unstable crown.
- The successive morphology transitions appear at lower values of the swirl ratio as the momentum ratio increases. A minimum value of M is needed to access morphologies different from the intact core. This translates to the transition lines between morphologies being more and more horizontal, as sketched in Fig. 9.

5. Discussion

This experimental study spans a wide range of flow conditions in a three-parameter space for the atomized spray: Re_l, M and SR. 19 independent experimental conditions were investigated, imaging a large portion of the spray near-field sequentially. Using high spatial and temporal synchrotron X-ray attenuation imaging, the internal details of the liquid structure were revealed, demarcating four different morphologies of the liquid jet during atomization. Imaging inside the nozzle through the atomizer walls shows, for instance, that liquid can wick upstream along the needle outer walls, despite the downstream high-speed gas jet inside the nozzle. Even for low values of the momentum ratio, when the spray formation is dominated by the bag break-up mechanism, the intact liquid core is highly non-axisymmetric, with short wavelength interfacial perturbations forming along the core, at different axial and azimuthal locations, simultaneously.

While most of these interfacial perturbations get elongated by the high-speed gas into ligaments or sheets and then experience break-up, we have demonstrated for the first time that they can reattach to the liquid core and entrap air bubbles in the process. The air bubbles are then advected downstream by the accelerating liquid jet, and can be found in thin liquid sheets, ligaments and droplets. They induce local changes in surface energy on the liquid that is already experiencing gas-induced turbulent stresses, but their exact role in the break-up process remains to be determined. The entrainment efficiency, measured in terms of projected bubble surface fraction, is shown to be an increasing function of the momentum ratio and a decreasing function of swirl ratio at high values of M. This could be related to a decrease of the liquid core stability that precipitates drastic changes in its morphology.

The liquid jet follows three different morphologies for momentum ratios at or above 100: a partially hollowed crown with ligaments shedding from its rim, a complete 360° liquid crown that partially detaches for a small portion of the liquid needle circumference in partial dewetting, and a partial 120 − 180° liquid crown detached for a large portion of the needle circumference. The combination of surface tension and liquid acceleration allows the liquid core to bridge the detachment upstream of the break-up region in the third morphology described. On the contrary, when swirl is added at high momentum ratios, the liquid crown reduces its extent and is only attached to the rim at a azimuthal length of 120 − 180°, pushed by what we believed is a gas recirculation cavity that is seen to penetrate upstream, inside the liquid needle. This is a novel observation that is only possible due to the use of high energy synchrotron X-ray imaging that penetrates and images

through the atomizer (liquid needle and gas nozzle) walls. The instability of this cavity must govern the observed rotational motion of the attachment length of the partial crown. The projection of the crown's center of mass location in the y axis shows a bi-modal PDF, with a characteristic time of rotation along the needle circumference that is long compared to the flow timescales. This bi-modal PDF exists when swirl is present and is an increasing function of both momentum and swirl ratios.

6. Conclusions

Using high-speed X-ray imaging of the inner details of the spray core region, unexpected phenomena have been revealed for the first time that include air bubble entrapment by the liquid core, wicking of the liquid upstream inside the nozzle along the outer walls of the liquid needle, and entrainment of gas inside the liquid needle for a significant percentage of the liquid needle cross-section. The liquid jet, initially intact at low gas momentum ratios, becomes hollow in its center for high gas momentum ratios, and is subject to dewetting and rotational motion when swirl is added in the gas flow. Four different morphologies of the liquid core are identified, and shown to depend solely on two flow parameters. From observations of the high-speed X-ray imaging and the first quantitative analyses presented above, a phase diagram is drawn to determine the liquid core morphology in a quantitative way, in terms of the swirl and gas-to-liquid momentum ratios. The threshold for the transition from partial dewetting to unstable crown in terms of swirl ratio, is a decreasing function of the momentum ratio. In the same manner, transition in liquid core morphologies happens at much lower values of the momentum ratio as swirl increases. While, in the absence of swirl, the liquid Reynolds number is known to impact the liquid intact length (Chigier and Reitz, 1996), and the spray droplet size (Aliseda et al., 2008), this study shows clearly that it is not a relevant parameter to describe the liquid core regimes, as these are fully described by the parameter space (M, SR).

Further studies to obtain more converged statistics of break-up events in the presence of bubbles in liquid sheets and droplets, as well as on wicking and gas penetration events for a range of experimental conditions are needed. Complementary velocity measurements, such as implemented by Descamps et al. (2008); Rajamanickam and Basu (2017), would help better understand the underlying mechanisms responsible for the change in liquid core morphologies. Finally, modeling of the gas and liquid boundary layers that takes into account the liquid core morphology would shed light into how to improve spray instabilities and droplet size predictions.

Acknowledgements

References

Aliseda, A., Hopfinger, E.J., Lasheras, J.C., Kremer, D.M., Berchielli, A., Connolly, E.K., 2008. Atomization of viscous and non-newtonian liquids by a coaxial, high-speed gas jet. experiments and droplet size modeling. Int. J. Multiphase Flow 34 (2), 161–175.

Bothell, J.K., Li, D., Morgan, T.B., Heindel, T.J., Aliseda, A., Machicoane, N., Kastengren, A.L., 2018. Characterizing the near-field region of a spray using white beam and focused beam X-ray measurements. In: Institute for Liquid Atomization and Spray Systems. ICLASS 2018, 14th Triennial International Conference on Liquid Atomization and Spray Systems, Chicago, IL, USA, July 22–26, 2018.

Chigier, N., Reitz, R.D., 1996. Regimes of jet breakup and breakup mechanisms-physical aspects. Recent Adv.Spray Combust. 1, 109–135.

Delon, A., Cartellier, A., Matas, J.P., 2018. Flapping instability of a liquid jet. Phys. Rev. Fluids 3 (4), 043901.

Descamps, M., Matas, J.P., Cartellier, A., 2008. Gas-liquid atomisation: gas phase characteristics by PIV measurements and spatial evolution of the spray. In 2nd colloque INCA, Initiative en Combustion Avancée (p. 1).

Halls, B.R., Radke, C.D., Reuter, B.J., Kastengren, A.L., Gord, J.R., Meyer, T.R., 2017. High-speed, two-dimensional synchrotron white-beam x-ray radiography of spray breakup and atomization. Opt. Express 25 (2), 1605–1617.

Heindel, T.J., 2011. A review of x-ray flow visualization with applications to multiphase flows. ASME J. Fluid Eng. 133 (7), 074001.

Heindel, T.J., 2019. X-Ray imaging techniques to quantify spray characteristics in the near-field. Atomizat. Sprays 29 (1), 028797.

Heindel, T.J., Li, D., Morgan, T.B., Bothell, J.K., Aliseda, A., Machicoane, N., Kastengren, A.L., 2017. X-ray observations in the spray near-field using synchrotron x-rays. In: Institute for Liquid Atomization and Spray Systems. ILASS-Americas 29th Annual Conference on Liquid Atomization and Spray Systems, Atlanta, GA, May 15–18, 2017.

Hopfinger, E.J., Lasheras, J.C., 1996. Explosive breakup of a liquid jet by a swirling coaxial gas jet. Phys. Fluids 8 (7), 1696–1698.

Huck, P.D., Machicoane, N., Osuna-Orozcon, R., Aliseda, A., 2018. Experimental characterization of a canonical two-fluid coaxial atomizer. In: Institute for Liquid Atomization and Spray Systems. ICLASS 2018, 14th Triennial International Conference on Liquid Atomization and Spray Systems, Chicago, IL, USA, July 22–26, 2018.

Kastengren, A.L., Powell, C.F., 2014. Synchrotron x-ray techniques for fluid dynamics. Exp. Fluids 55 (3), 1686.

Kastengren, A.L., Powell, C.F., Arms, D., Dufresne, E.M., Gibson, H., Wang, J., 2012. The 7BM beamline at the APS: a facility for time-resolved fluid dynamics measurements. J. Synchrotron. Radiat. 19 (4), 654–657.

Lasheras, J.C., Hopfinger, E.J., 2000. Liquid jet instability and atomization in a coaxial gas stream. Annu. Rev. Fluid. Mech. 32 (1), 275–308.

Lasheras, J.C., Villermaux, E., Hopfinger, E.J., 1998. Break-up and atomization of a round water jet by a high-speed annular air jet. J. Fluid. Mech. 357, 351–379.

Linne, M.A., Paciaroni, M., Berrocal, E., Sedarsky, D., 2009. Ballistic imaging of liquid breakup processes in dense sprays. Proc. Combust. Inst. 32 (2), 2147–2161.

Machicoane, N., Osuna-Orozco, R., Huck, P.D., Aliseda, A., 2018. Experimental investigation of multi-physics control of a two-fluid coaxial atomizer. In: Institute for Liquid Atomization and Spray Systems. ICLASS 2018, 14th Triennial International Conference on Liquid Atomization and Spray Systems, Chicago, IL, USA, July 22–26, 2018.

Marmottant, P., Villermaux, E., 2004. On spray formation. J. Fluid Mech. 498, 73–111.

Rajamanickam, K., Basu, S., 2017. Insights into the dynamics of spray swirl interactions. J. Fluid Mech. 810, 82–126.

Tennekes, H., Lumley, J.L., 1972. A First Course in Turbulence. MIT press, Cambridge, Massachusetts.

Varga, C.M., Lasheras, J.C., Hopfinger, E.J., 2003. Initial breakup of a small-diameter liquid jet by a high-speed gas stream. J. Fluid Mech. 497, 405–434.

Yue, Y., Powell, C.F., Poola, R., Wang, J.C., Schaller, J.K., 2001. Quantitative measurements of diesel fuel spray characteristics in the near-nozzle region using x-ray absorption. Atomization Spray. 11 (4).